Makara Journal of Science

Volume 27
Issue 1 *March*

Article 3

3-25-2023

Carbon dioxide-Induced Corrosion of AISI 4140 Steel in Acidified Artificial Geothermal Brine

Anawati Anawati
Department of Physics, Faculty of Mathematics and Natural Sciences, Universitas Indonesia, Depok 16424, Indonesia, anawati@sci.ui.ac.id

Rayhan Izzat
Department of Physics, Faculty of Mathematics and Natural Sciences, Universitas Indonesia, Depok 16424, Indonesia

Riene Kaelamanda Pragitta
Department of Physics, Faculty of Mathematics and Natural Sciences, Universitas Indonesia, Depok 16424, Indonesia

Rafli Ihsan Hernandi
Department of Physics, Faculty of Mathematics and Natural Sciences, Universitas Indonesia, Depok 16424, Indonesia

Makara Journal of Science, 27/1 (2023), 19–24
doi: 10.7454/mss.v27i1.1451

Carbon dioxide-Induced Corrosion of AISI 4140 Steel in Acidified Artificial Geothermal Brine

Anawati Anawati*, Rayhan Izzat, Riene Kaelamanda Pragitta, and Rafli Ihsan Hernandi

Department of Physics, Faculty of Mathematics and Natural Sciences, Universitas Indonesia, Depok 16424, Indonesia

*E-mail: anawati@sci.ui.ac.id

Received October 25, 2022 | Accepted Februari 9, 2023

Abstract

Carbon dioxide (CO_2)-induced corrosion often occurs in the structural materials of geothermal industry. The presence of CO_2 influences the formation of various corrosion products. This research investigates the effect of dissolved CO_2 in acidic brines on the corrosion behavior of AISI 4140 steel at atmospheric pressure. The brines were the standard brine, Ca-free brine, and high-salinity brine. The corrosion behavior was studied using electrochemical and immersion tests. A cyclic polarization test showed that the corrosion rate was higher in dissolved CO_2 brine than in non-CO_2 brine, and an immersion test demonstrated a similar result. In the absence of CO_2, the presence of Ca ions in the brine reduced the corrosion rate of the alloy from 26.8 to 24.6 mmpy and further to 20.7 mmpy in the high-salinity brine. A similar trend was demonstrated during immersion in the CO_2-containing brine, with higher rates of 37.1, 30.9, and 24.9 mmpy for the Ca-free, standard, and high-salinity brines, respectively. However, the Ca ions and high-salinity brines induced a more localized corrosion as pit and filiform. A surface analysis using an optical microscope revealed that immersion in CO_2 brines generated 4–10-fold higher surface roughness than the non-CO_2 brines. In all specimens, a protective layer was not established during the tests. No new phase was detected using X-Ray diffractometer after the immersion test. Moreover, no tendency of passivation was observed in the reverse scan of the cyclic polarization test.

Keywords: acidizing, corrosion, polarization, XRD

Introduction

The geothermal industry uses AISI 4140 steel, such as chromium–molybdenum carbon steel, in wellhead components [1, 2]. Exposure to a geothermal environment and elevated temperature corrodes the pipe wall components. Carbon dioxide (CO_2) corrosion is a problem in the geothermal industry because of its nature, which accelerates the corrosion rate. Dissolved CO_2 decreases the pH because of the formation of carbonic acid (H_2CO_3) [3]. CO_2 corrosion was identified as a uniform corrosion that causes the thinning of the wall, casings, pipes, and other equipment. The reduction in wall thickness is dangerous because it may lead to fracture and failure of the material. The accumulation of corrosion products as $FeCO_3$ on the surface was reported [4] to reduce the corrosion rate. Other phases that can act as protective layers were also identified, including Fe_3O_4, Fe_3C, $Fe_2O_2CO_3$, and Fe_2O_3 [5]. The formation of protective oxide was affected by several factors, such as solution pH, ionic composition, and CO_2 presence in the solution. However, most of the studies were performed in neutral and alkaline environments in which the dissolved CO_2 tended to decrease the pH substantially. Reports on CO_2-induced corrosion at low pH are lacking.

AISI 4140 is an alloy steel containing the primary alloying elements chromium and molybdenum. In the formation of the passive layer, an essential element is chromium. Molybdenum acts as a protective film stabilizer in an environment with chloride ions (Cl^-) [6]. Fe metal is oxidized to form Fe^{+2} and then migrates toward the cathode and reacts with OH^- to form basic oxides, namely, ferrous hydroxide, which can react again with Fe^{+2} to produce a precipitate in the form of rust. However, less dissolved oxygen produces less deposit in a high-salinity environment [7].

To remove mineral scale, geothermal wells are commonly subjected to acidizing treatment using HCl in concentrations ranging from 0.05% to 30% for up to 60 h [8–10]. However, this treatment can increase the corrosion rate in wells made of carbon steel casing, but to date, few studies have focused on the effects of saturated CO_2 gas on geothermal brine under acidizing conditions. A 35 °C temperature simulates the temperature of a low-enthalpy system injection well, where the particular system limits its temperature to < 90 °C [11, 12]. The effect of brine composition on the behavior of the CO_2-induced corrosion of geothermal wells under acidizing conditions must be studied. In this

work, the corrosion behavior of AISI 4041 under acidizing conditions is investigated using three variations of brine with different compositions.

Materials and Methods

Materials. The specimens used for this research were commercial AISI 4140 steel billets. The billets were cut into small cylinders with a diameter of 25 mm and a thickness of 10 mm. The specimens were molded in resin. The specimens were ground with #80, #600, #1200, and #2000 SiC sandpapers on a rotary polisher at 300 rpm until the test surface was mirror-finished. Last, the samples were cleaned in deionized (DI) water using an ultrasonic cleaner and dried.

Brine preparation. Six types of brine with different compositions were used for the corrosion test. The compositions are listed in Table 1. The brine was prepared from salt powders of NaCl, KCl, and $CaCl_2$ from Merck. The powders were poured consecutively into DI water in a beaker glass. Next, the salt powders were dissolved, and the solution pH was set to 2.0 by adding hydrochloric acid (HCl). The mixed solution was stirred at room temperature in ambient air for 30 min before further use. The brine was then separated into two sealed containers, one for the non-CO_2 brine and the other for the CO_2 brine. Before the polarization corrosion test was performed, the non-CO_2 and CO_2 brines were heated to a boiling temperature (100 °C) at atmospheric pressure to reduce the amount of dissolved oxygen in the solution. The solution was then cooled to room temperature. The pH was measured and showed a decrease from 2.0 to 1.2 after the CO_2 bubbling process. The dissolved CO_2 was introduced by bubbling CO_2 gas into the solution for 2 h before the test. The specimen mass was weighed before and after the immersion.

Corrosion tests. The corrosion tests were performed through immersion and polarization tests. These tests were replicated on three specimens. The immersion test was performed for 24 h in a sealed container. The specimen was then washed in DI water and dried. The polarization test was performed in a cyclic potentiodynamic mode using a potentiostat Corrtest CS310. The electrochemical cell used three electrodes: the specimen as the working electrode, a platinum mesh as the counter electrode, and a saturated Ag/AgCl electrode as the reference electrode. The cycle started with the first sweep from the negative potential to the positive potential and vice-versa for the second sweep at a scan rate of 0.5 mV/s. The corrosion current density and corrosion potential were determined by Tafel extrapolation using Corrtest C5 software. The corrosion rate was calculated using Equation (1).

$$\text{Corrosion rate (mmpy)} = 1/\rho\ (K \times \text{Icorr} \times EW), \qquad (1)$$

where K is a constant, 3.27×10^{-3}, I_{corr} is the corrosion current density ($\mu A/cm^2$), EW is the equivalent weight, which is 18.558 for AISI 4140 steel [13], and ρ is the material density (g/cm^3).

Table 1. Brine Composition in 1 L Solution

Brine code	NaCl (mg/L)	KCl (mg/L)	$CaCl_2$ (mg/L)	HCl (mL)	CO_2
B1	28.548	5.960	-	14	No
B2	28.548	5.960	-	14	Yes
B3	28.548	5.960	2.664	2	No
B4	28.548	5.960	2.664	2	Yes
B5	40950	5960	2664	7	No
B6	40950	5960	2664	7	Yes

Characterization. The surface observation was proceeded using an optical microscope (Zeiss). To reveal the microstructure, the specimen was etched using Kalling's reagent. For surface roughness measurements, a digital microscope (Keyence VHX7000) was used. The phases in the specimen were analyzed using an X-Ray diffractometer (XRD, X`pert Pro MPD PANalytical). The XRD machine had a Cu-Kα ray source and the diffraction angle (2θ) used was $20° < 2\theta < 90°$. The data were analyzed using Match! and FullProf Suite software to determine the phase.

Results and Discussion

The microstructure of AISI4140 is displayed in Figure 1. The structure comprised dark and bright areas. The microstructure is similar to that reported earlier [14] in that it comprises pearlite (two-phased) and ferrite phases. The pearlite appeared as a lamellar arrangement of the two-phase ferrite and cementite system and hence appeared darker. Meanwhile, the ferrite phase appeared bright.

The cyclic potentiodynamic polarization of the alloy is depicted in Figure 2. The forward cycle scanned the potential from the negative to the positive direction and the opposite for the reverse cycle. In the forward scan, the

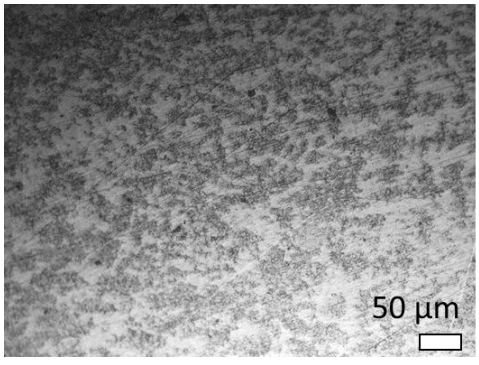

Figure 1. Microstructure of AISI 4041

corrosion potential of the alloy in the Ca-free brines (B1 and B2) was approximately similar to that in high-salinity brines (B5 and B6) at −0.43 VAg/AgCl. Meanwhile, in the standard brine, the corrosion potential was slightly nobler at −0.39 and −0.37 VAg/AgCl, respectively. The Tafel extrapolation parameters are listed in Table 2. The corrosion potential and current density were obtained by extrapolating the linear part in the cathodic and anodic curves near their intersection. The slopes of the corresponding fitted linear lines are βc (cathodic) and βa (anodic). The corrosion potential (Ecorr) represents the ease in which a metallic surface undergoes corrosion. The corrosion potential was in the range of that obtained in simulated seawater at pH 8.4 reported earlier [14]. The results indicated that the effect of solution pH on the corrosion potential was unsubstantial. In contrast, the brine composition affected the corrosion current density (icorr). The current density represents the number of metallic ions released from the specimen into the solution. The polarization curves for the CO_2-containing brines were shifted to higher current densities relative to those for the non-CO_2 brines. Consequently, the corrosion current density of the alloy was slightly higher in the CO_2-containing brines than in the CO_2-free brines, as listed in Table 2.

The reverse sweep slightly shifted the polarization curve toward a higher current density, meaning a higher corrosion rate. These results indicated that AISI 4140 steel was further corroded during the reverse sweep. No tendency of passivation was displayed by the specimens in all types of brine used in this work. This phenomenon revealed that no protective layer was developed on the specimen surface. The behavior of the non-protective surface layer of steel has been reported [15]. The low pH of the brine triggered a continuous dissolution of the metal surface, inhibiting the deposition of the corrosion product. The corrosion product was completely dissolved in the brine. The brine became considerably dirty (brownish) after the polarization test of each specimen. Therefore, the brine was used only for the one-time test. The mirror surface appearance of the specimen turned black after the polarization test.

The corrosion current density from the forward scan of the polarization curve was converted into the corrosion rate using Equation (1). The results are plotted as a function of the brine sample in Figure 3. The corrosion rates in CO_2-containing brines (B2, B4, and B6) are consistently higher than those in CO_2-free brines (B1, B3, and B5). Dissolved CO_2 helped enhance the corrosion rate by decreasing the pH. The corrosion rate increased with decreasing pH [10]. The lower corrosion rate in B1 and B4 relative to B1 and B2 was due to the absence of Ca ions in the brines. The Ca ions accelerated the corrosion of an iron-based metal, particularly in the presence of dissolved CO_2 in a chloride-containing solution [16]. The carbonate ions from the dissolved CO_2 attacked the metal surface and formed $FeCO_3$. At high Ca content in the solution, $FeCO_3$ scale may develop on the surface [5]. This scale was, however, non-protective and enhanced the corrosion rate by initiating the pit. Therefore, the corrosion rate was lower in the non-Ca-containing brine. The high salinity in B5 and B6 suppressed the dissolved oxygen content in the brines. The limited oxygen content lowered the cathodic reaction and depressed the corrosion rate of iron.

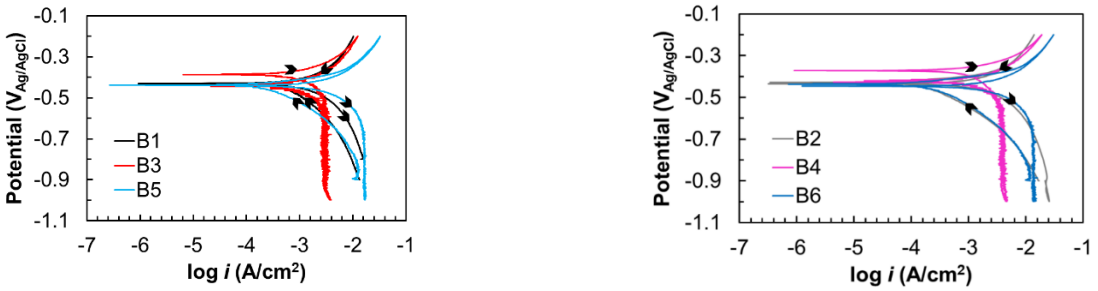

a) b)

Figure 2. Potentiodynamic Polarization of AISI 4140 in a) Non-CO_2 Brines (B1, B3, B5) and b) CO_2 Brines (B2, B4, B6)

Table 2. Corrosion Potentials and Current Densities Analyzed from the Forward Scan Polarization Curves in Figure 2

Specimen	βc (V/dec)	βa (V/dec)	Ecorr ($V_{Ag/AgCl}$)	*i*corr (A/cm²)
B1	−0.061	0.043	−0.43	3.47×10^{-3}
B2	−0.068	0.038	−0.43	4.80×10^{-3}
B3	−0.021	0.031	−0.39	3.18×10^{-3}
B4	−0.039	0.026	−0.37	3.99×10^{-3}
B5	−0.027	0.023	−0.43	2.68×10^{-3}
B6	−0.036	0.020	−0.43	3.22×10^{-3}

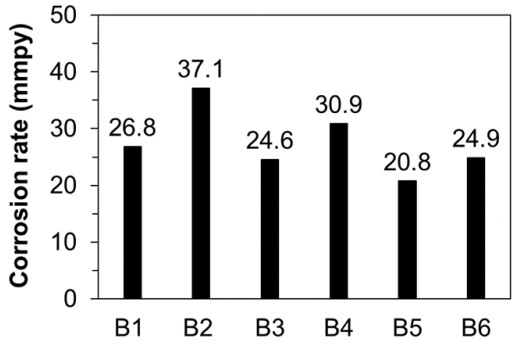

Figure 3. Corrosion Rate of AISI 4140 in Brines B1–B6 Calculated from Cyclic Polarization

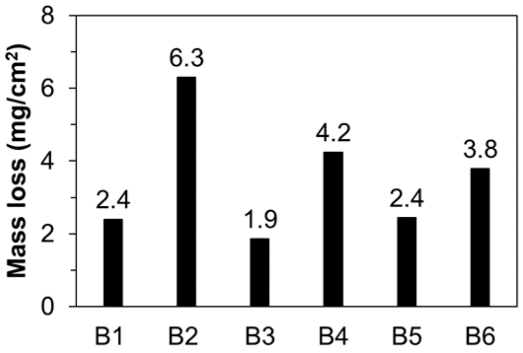

Figure 4. Mass Loss of AISI 4140 in Brines B1–B6 for 24 h

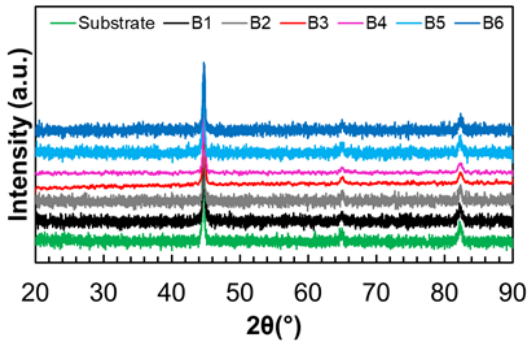

Figure 5. XRD Patterns of AISI 4140 After the Corrosion Test in Brines B1–B6

To validate the results of the cyclic polarization test, the corrosion behavior of AISI 4140 was investigated using an immersion test in the corresponding brines for 24 h in ambient air. The relatively short immersion time does not allow for the conversion of mass loss into mmpy. Figure 4 shows the mass loss in the variation of the brines. The mass loss trend in Figure 4 agrees with Figure 3. The specimen exhibited higher mass loss, indicating a higher corrosion rate, in the brine containing CO_2 (B2, B4, and B6) than in the non-CO_2 brine (B1, B3, and B5). Additionally, a reduction of mass loss was observed in the Ca-free brines and a further decrease in high-salinity brines relative to the standard brines (B1 and B2).

Figure 5 shows the XRD patterns of the specimens after immersion in the brines for 24 h. The peaks for the substrate were identified at 45.1°, 65.3°, and 82.6°, corresponding to the Fe phase. These three peaks, referred to as the Fe phase, appeared in the spectra of all specimens after immersion. No additional peak was detected in the spectra of the specimens after immersion in the corrosive brines (B1–B6). These results indicated that no corrosion product was deposited on the surface. The corrosion product was also not detected in the brine containing dissolved CO_2. The high corrosion rate was the main factor that hindered the deposition of detectable corrosion products. Another reason was possibly the short duration of immersion. $FeCO_3$ precipitated slowly at atmospheric pressure and 35 °C [3], consistent with the cyclic polarization test that demonstrated no passivation behavior on forward and reversed scans.

The corrosion morphology of AISI 4140 after immersion for 24 h in the brines is displayed in Figure 6. All the specimens revealed a rough surface with a deposited layer that appeared red-brownish, a typical color for rust. The rust was possibly developed during storage in the laboratory. Although we placed the specimens in a dry box, their access to air remained free. Oxidation in a dry environment might have occurred. The damage caused by corrosion in the CO_2-containing brine (Figures 6b, 6d, and 6f) was more severe, resulting in a darker appearance and more corroded features than in the CO_2-free brine (Figures 6a, 6c, and 6e). Despite the uniform corrosion, a deeper attack as filiform corrosion is observed in Figure 6b. Filiform corrosion is a common type of corrosion on painted metal, particularly steel. It can also occur on a surface covered by an oxide layer. Filiform corrosion is initiated at cracks in the surface layer and propagates omni directionally, forming a thread-like shape under the surface layer [17]. The head is the active sites (anodic part) while the corrosion product accumulates at the tail (cathodic part). Despite the aesthetic aspect, filiform corrosion is considered milder than the other types of localized corrosion because the depth of attack is superficial. However, filiform corrosion may cause film delamination at a long exposure time to a corrosive environment [18]. Unlike corrosion in CO_2 brines, a uniform type of attack dominated corrosion in the CO_2-free brines, as revealed by Figures 6a, 6c, and 6d. The uniform corrosion produced a relatively low surface roughness below 10 μm, as tabulated in Table 3. The surface roughness was measured along the blue line in Figure 6. Meanwhile, the localized corrosion led to a higher surface roughness in the range of 13–41 μm. Localized corrosion, particularly pitting, tendangers the integrity of the metal, as it propagates into the bulk metal. The dissolved CO_2, which potentially forms carbonic acid, created a more aggressive environment that triggered additional localized corrosion in addition to uniform corrosion.

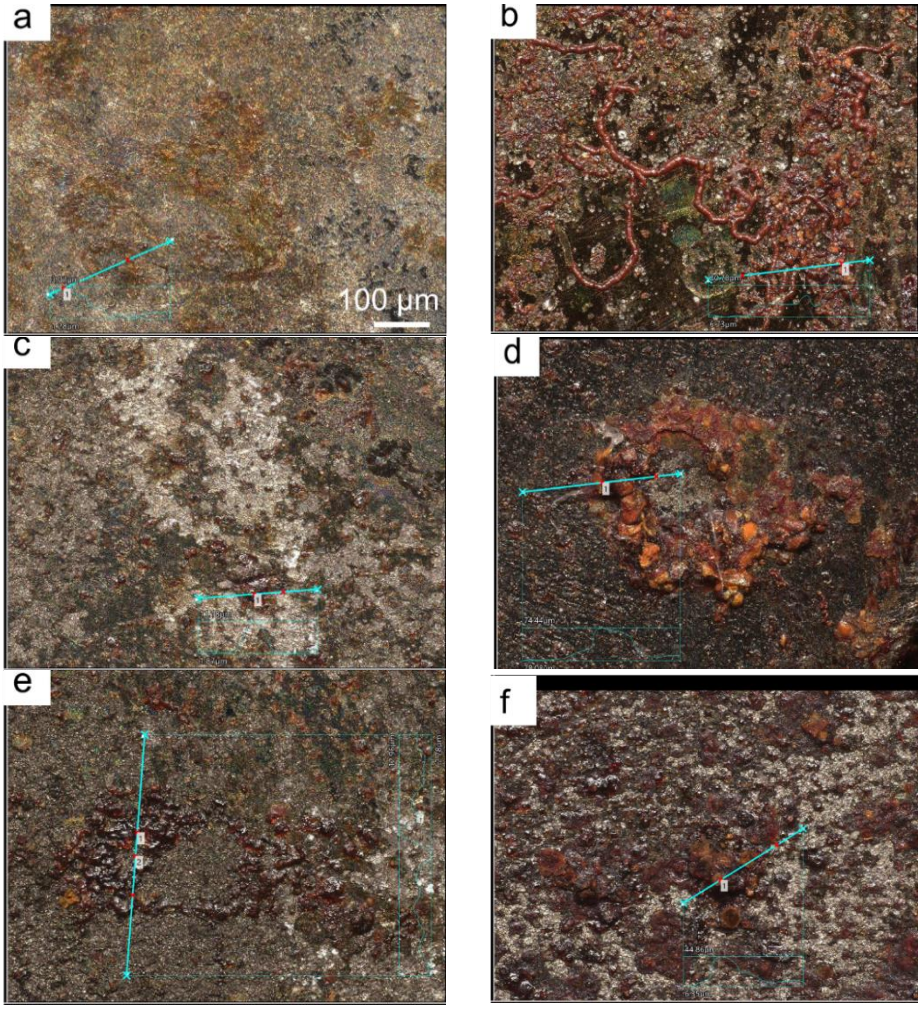

Figure 6. Corrosion Morphology of AISI 4140 After Exposure in Brines a) B1, b) B2, c) B3, d) B4, e) B5, f) and B6. The SCALE BAR in Image a was Applied to All Images

Table 3. Surface Roughness with the Line Analysis Shown in Figure 6

Specimen	Roughness (µm)
B1	1.52
B2	13.75
B3	9.18
B4	41.26
B5	6.52
B6	32.94

Conclusion

The corrosion behavior of AISI 4140 in six acidified geothermal brines was investigated. The brines containing saturated CO_2 damaged the specimen more severely than the non-CO_2 brines. Calculated from the cyclic polarization curve, the corrosion rate ranged from 25 to 37 mmpy and 21–27 mmpy for the specimen in CO_2-containing brine and non-CO_2 brines, respectively. In agreement, the mass loss measured during the immersion test was higher in CO_2-containing brines than in the CO_2-free brines. This higher corrosion rate was due to the lower pH, creating a more aggressive environment. The polarization test revealed no passivation tendency, indicating no protective layer formation. The XRD pattern confirmed that after the immersion test, no other phase aside from the iron phase was present in the specimen. The results suggested that the presence of dissolved CO_2 accelerated the corrosion of AISI 4140 and triggered localized corrosion. The localized corrosion produced a high surface roughness of 13–41 µm.

Acknowledgment

We acknowledge Kemendikbud-ristek through Hibah Penelitian Terapan Unggulan Perguruan Tinggi (PTUPT) No. NKB-828/UN2.RST/HKP.05.00/2022 for the financial support of this work.

References

[1] Rubiandini, R.R.S., Subiatmono, P., Buntoro, A., Supriyatman, D. 1999. Stress Corrosion Cracking: AISI 420, 4140, and 1045 on Alloy Steel Used in the Oil, Gas, and Geothermal Industry at Elevated Temperatures in a Hydrogen Sulfide Environment. Int. Symp. Oilfield Chem. SPE-50789-MS, https://doi.org/10.2118/50789-ms.

[2] Haryadi, G.D. 2006. Pengaruh Kecepatan Air Sirkulasi Sebagai Medium Quenching Terhadap Kekerasan dan Struktur Mikro Pada Baja AISI 4140. Rotasi. 8(1): 24–33, https://doi.org/10.14710/rotasi.8.1.24-33.

[3] Cui, G., Yang, Z., Liu, J., Li, Z. 2019. A comprehensive review of metal corrosion in a supercritical CO_2 environment. Int. J. Greenh. Gas Contr. 90: 102814, https://doi.org/10.1016/j.ijggc.2019.102814.

[4] Mundhenk, N., Knauss, K.G., Bandaru, S.R.S., Wonneberger, R., Devine, T.M. 2019. Corrosion of carbon steel and the passivating properties of corrosion films formed under high-PT geothermal conditions. Sci. Total Environ. 677: 307–14, https://doi.org/10.1016/j.scitotenv.2019.04.386.

[5] Barker, R., Al Shaaili, I., De Motte, R.A., Burkle, D., Charpentier, T., Vargas, S.M., Neville, A. 2019. Iron carbonate formation kinetics onto corroding and pre-filmed carbon steel surfaces in carbon dioxide corrosion environments. Appl. Surf. Sci. 469: 135–145, https://doi.org/10.1016/j.apsusc.2018.10.238.

[6] Dieter, G.E. 2000. Mechanical Metallurgy, 3rd ed. McGrawHill. United States.

[7] Narasimha, R. 2018. Corrosion Studies of Carbon Steel in 3% NaCl Solution in Presence of Expired Ceftin: Investigation of Environmental Friendly Corrosion Inhibitor. Iran. J. Energy Environ. 9(4): 295–298, https://doi.org/10.5829/ijee.2018.09.04.10.

[8] Osorio-Celestino, G.R., Hernandez, M., Solis-Ibarra, D., Tehuacanero-Cuapa, S., Rodríguez-Gómez, A., Gómora-Figueroa, A.P. 2020. Influence of Calcium Scaling on Corrosion Behavior of Steel and Aluminum Alloys. ACS Omega. 5: 17304–17313, https://doi.org/10.1021/acsomega.0c01538.

[9] Ventre, A., Ungemach, P. 1998. Soft Acidizing of Damaged Geothermal Injection Wells. Discussion of Result Achieved in the Paris Basin. Proc. Workshop Geoth. Reservotr Eng. 33–43.

[10] Aksoy, N., Serpen, U. 2010. Acidizing in Geothermal Wells and HCl Corrosion. Proc. World Geoth. Congr. 25–29.

[11] Rosca, M., Antics, M., Sferle, M. 2005. Geothermal Energy in Romania: Country Update 2000-2004. Proc. World Geoth. Congr. 24–29.

[12] Muffler, L.J.P. 1978. USGS Geothermal Resource Assessment United States, MS 18, U. S. Geological Survey, Menlo Park CA 94025.

[13] Hanza, S.S., Štic, L., Liverić, L., Špada, V. 2021. Corrosion Behaviour of Tempered 42CrMo4 Steel. Mater. Tehnol. 55(3): 427–433, https://doi.org/10.17222/mit.2021.014.

[14] Valdés, J., Huape, E., Oseguera, J., Ruíz, A., Ibarra, J., Bernal, J.L., Medina, A. 2022. Effects of plasma nitriding in the corrosion behavior of an AISI 4140 steel using a seawater medium solution. Mater. Lett. 316: 131991, https://doi.org/10.1016/j.matlet.2022.131991.

[15] Esmailzadeh, S., Aliofkhazraei, M., Sarlak, H. 2018 Interpretation of Cyclic Potentiodynamic Polarization Test Results for Study of Corrosion Behavior of Metals: A Review. Prot. Met. Phys. Chem. Surf. 54: 976–989, https://doi.org/10.1134/S207020511805026X.

[16] Shamsa, A., Barker, R., Hua, Y., Barmatov, E., Hughes, T.L., Neville, A. 2019. The role of Ca^{2+} ions on Ca/Fe carbonate products on X65 carbon steel in CO_2 corrosion environments at 80 and 150 °C. Corros. Sci. 156: 58–70, https://doi.org/10.1016/j.corsci.2019.05.006.

[17] Duret-Thual, C. 2014, 1 - Understanding corrosion: basic principles. In Liengen, T., Féron, D., Basséguy, R., Beech, I.B. (eds.), Understanding Biocorrosion. Woodhead Publishing. Cambridge. pp. 3–32.

[18] Brau, F., Thouvenel-Romans, S., Steinbock, O., Cardoso, S.S.S., Cartwright, J.H.E. 2019. Filiform corrosion as a pressure-driven delamination process. Soft Matter. 15: 803–812, https://doi.org/10.1039/C8SM01928B.